Seasonal Variation of Cloud Systems over ARM SGP

XIAOQING WU AND SUNWOOK PARK

Department of Geological and Atmospheric Sciences, Iowa State University, Ames, Iowa

QILONG MIN

Atmospheric Sciences Research Center, University at Albany, State University of New York, Albany, New York

ABSTRACT

Increased observational analyses provide a unique opportunity to perform years-long cloud-resolving model (CRM) simulations and generate long-term cloud properties that are very much in demand for improving the representation of clouds in general circulation models (GCMs). A year 2000 CRM simulation is presented here using the variationally constrained mesoscale analysis and surface measurements. The year-long (3 January–31 December 2000) CRM surface precipitation is highly correlated with the Atmospheric Radiation Measurement (ARM) observations with a correlation coefficient of 0.97. The large-scale forcing is the dominant factor responsible for producing the precipitation in summer, spring, and fall, but the surface heat fluxes play a more important role during winter when the forcing is weak. The CRM-simulated year-long cloud liquid water path and cloud (liquid and ice) optical depth are also in good agreement (correlation coefficients of 0.73 and 0.64, respectively) with the ARM retrievals over the Southern Great Plains (SGP). The simulated cloud systems have 50% more ice water than liquid water in the annual mean. The vertical distributions of ice and liquid water have a single peak during spring (March–May) and summer (June–August), but a second peak occurs near the surface during winter (December–February) and fall (September–November). The impacts of seasonally varied cloud water are very much reflected in the cloud radiative forcing at the top-of-atmosphere (TOA) and the surface, as well as in the vertical profiles of radiative heating rates. The cloudy-sky total (shortwave and longwave) radiative heating profile shows a dipole pattern (cooling above and warming below) during spring and summer, while a second peak of cloud radiative cooling appears near the surface during winter and fall.

1. Introduction

Cloud systems have long been recognized as an important factor for numerical weather prediction (NWP) and climate models. Convection and clouds affect large-scale circulations and wave disturbances such as the Madden–Julian oscillation (MJO) through the release of latent heat; the redistribution of heat, moisture, and momentum; and the precipitation. The large-scale forcing influences and modulates the development and organization of convection and clouds. The coupling of convective processes with the large-scale dynamics is crucial for modeling the seasonal variation and global distribution of precipitation, the MJO, and wave distur-

bances, and the atmosphere–ocean interaction (e.g., Miller et al. 1992; Slingo et al. 1994, 1996; Zhang et al. 1998; Maloney and Hartmann 2001; Lau and Waliser 2005; Zhang 2005). However, the great uncertainty in the parameterization of convection and clouds has limited the success in reproducing observations by general circulation models (GCMs). The lack of observations of cloud properties under different climate regimes does not help address the issues such as what processes control the activation of convection. The vertical and horizontal distributions of clouds affect the atmospheric radiation budgets through the reflection, absorption, and emission of radiation. With horizontal resolutions of several hundred kilometers in GCMs, the parameterization of cloud vertical overlap and horizontal inhomogeneity has been a challenging problem for improving radiation schemes (e.g., Manabe and Strickler 1964; Geleyn and Hollingsworth 1979; Stephens 1984; Cahalan et al. 1994; Liang and Wang 1997; Li et al. 2005).

Corresponding author address: Dr. Xiaoqing Wu, Iowa State University, 3010 Agronomy Hall, Ames, IA 50011.
E-mail: wuxq@iastate.edu

The inclusion of subgrid cloud variability in the radiation calculation for GCMs requires the knowledge of cloud statistics under different climate regimes, which is not yet available from observations.

The cloud-resolving model (CRM) provides a useful tool to simulate cloud systems under various large-scale conditions and over different regions. Week- and month-long CRM simulations have been conducted using the large-scale forcing from several field experiments including Global Atmospheric Research Program Atlantic Tropical Experiment (GATE), Tropical Ocean and Global Atmosphere Coupled Ocean–Atmosphere Response Experiment (TOGA COARE), and Atmospheric Radiation Measurement Program (ARM). While the direct validation of CRM-produced cloud systems still requires measurements of cloud properties, the evaluation of model-produced ensemble statistics including radiative fluxes, precipitation, and surface heat fluxes against observational estimates suggested that a desirable degree of realism has been reached for simulated clouds (e.g., Grabowski et al. 1996; Wu et al. 1998, 2007a; etc.). The CRM-simulated cloud-scale properties have shown great value for improving the representation of cloud-related processes in GCMs such as the parameterization of convective momentum transports and the inclusion of subgrid cloud distribution in the radiation calculation (e.g., Zhang and Wu 2003; Wu et al. 2003; Liang and Wu 2005; Wu and Liang 2005; Wu et al. 2007a,b). CRMs have also been used as a superparameterization to replace the convection and cloud parameterization schemes in GCMs for simulating the interaction of convection and clouds with large-scale circulation (e.g., Grabowski 2001; Randall et al. 2003).

While CRMs have been increasingly used by many studies, the available large-scale forcing data are limited. The field experiments like GATE, TOGA COARE, and ARM Intensive Operational Periods (IOPs) only last a few months at few locations. Consequently, CRM-simulated cloud systems are not necessarily generalized for different large-scale conditions. Since many observations are point measurements, longer integrations of CRM will provide more robust statistical analysis for the validation of model-produced cloud properties. Recently, multiyear-long forcing data over the ARM Southern Great Plains (SGP) site were constructed by a variational analysis using the mesoscale analysis and the ARM measurements at the surface and the top of the atmosphere (TOA; Xie et al. 2004). A series of single-column model (SCM) simulations were performed by Xie et al. using these forcing data. To avoid systematic drift in temperature and moisture, the SCM runs were initiated every day (e.g.,

Ghan et al. 2000). However, the year-long CRM simulation presented in this paper is forced continuously and allows the investigation of spatial and temporal variability of cloud and radiative properties.

The objective of this study is to evaluate the performance of year-long CRM simulations of cloud systems over the ARM SGP site for the first time and to examine the seasonal variation of cloud and radiative properties. The CRM-produced cloud properties and the large-scale forcing data should provide a valuable long-term dataset for understanding the characteristics of convective, cloud, and radiative processes, and the interaction between these subgrid-scale processes in GCMs. The successful integration of CRMs will also support the use of a similar approach to produce the long-term forcing data for different climate regimes, provided the long-term surface and TOA measurements are available together with mesoscale analyses such as the National Oceanic and Atmospheric Administration (NOAA) Rapid Update Cycle (RUC) analyses. In the next section, the Iowa State University (ISU) CRM will be introduced and the large-scale forcing datasets and experimental setup will be described. CRM-simulated cloud and radiative properties of midlatitude cloud systems such as ice water paths, radiative heating rates, and their seasonal variability will be presented in section 3. A summary will be given in section 4.

2. Cloud-resolving model, observational data, and experimental design

The CRM is a two-dimensional version of the Clark–Hall anelastic cloud model (e.g., Clark et al. 1996) with the imposed large-scale forcing and the modifications to physical processes important for the long-term simulations of cloud systems (e.g., Grabowski et al. 1996; Wu et al. 1998, 1999; Wu and Moncrieff 2001). The microphysical processes are treated by the Kessler (1969) bulk warm rain parameterization and the Koenig and Murray (1976) bulk ice parameterization. The ice scheme predicts two types of ice particles, that is, type A ice of slowly falling and low-density (unrimed or lightly rimed) particles, and type B ice of fast-falling and high-density graupel. Each type of ice is represented by two variables (i.e., mixing ratio and number concentration). The radiative process is handled by the radiation scheme of the National Center for Atmospheric Research (NCAR) Community Climate Model (CCM; Kiehl et al. 1996) with the use of binary liquid and type A ice clouds, which have effective radii of 10 and 30 μm, respectively. The subgrid-scale mixing is parameterized using the first-order eddy diffusion
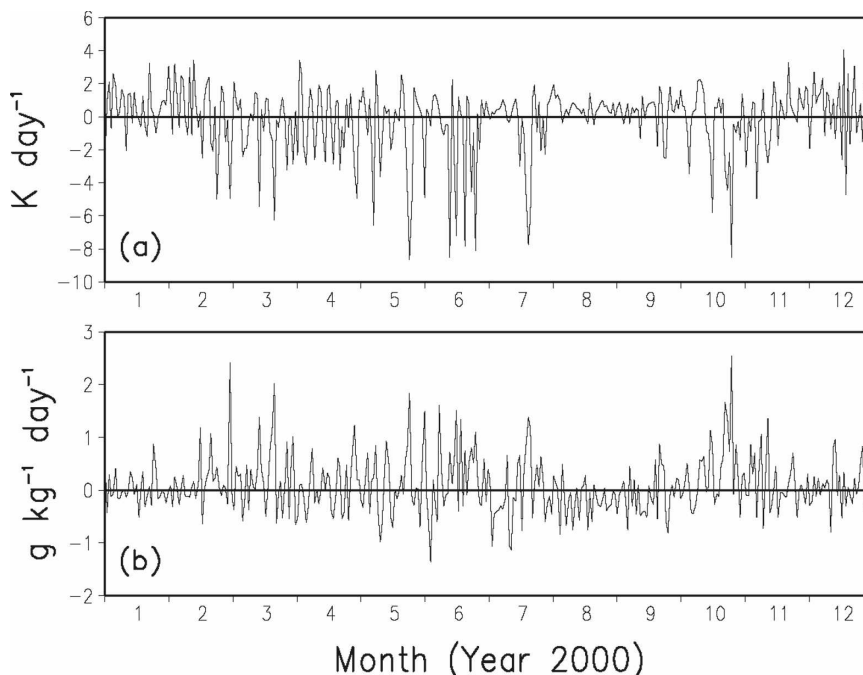
FIG. 1. Year-long (3 Jan–31 Dec 2000) evolution of vertically integrated daily (top) temperature and (bottom) moisture forcing over the ARM SGP.

method of Smagorinsky (1963). A nonlocal vertical diffusion scheme (Troen and Mahrt 1986; Holtslag and Moeng 1991; Hong and Pan 1996) is used to distribute the surface latent and sensible heat fluxes within the boundary layer.

The year-long (3 January–31 December 2000) hourly large-scale forcing data obtained from the ARM archive (available online at http://iop.archive.arm.gov/) is constructed using the variational analysis of NWP model-produced fields constrained by surface and TOA observations over the ARM SGP site including precipitation, latent and sensible heat fluxes, and radiative fluxes (Xie et al. 2004). Figure 1 presents the evolution of vertically integrated daily temperature and moisture forcing over the ARM SGP site during the year 2000. The forcing indicates a clear seasonal variation with stronger advective cooling (negative values in Fig. 1a) in summer [June–August (JJA)] and spring [March–May (MAM)], and weaker advective cooling in winter [December–February (DJF)] and fall [September–November (SON)]. The stronger advective cooling is generally correspondent with the stronger advective moistening (positive values in Fig. 1b). The seasonal variation is further shown in the vertical distributions of temperature and moisture advective forcing (Fig. 2). Large cooling is located between 4 and 10 km with a peak around 7 km in JJA and MAM, while the cooling is smaller in SON with virtually no tropospheric cooling

in DJF (Fig. 2a). Advective moistening exists above 1 km in MAM, SON, and DJF but above 2 km in JJA (Fig. 2b). The large advective drying below 2 km in JJA is largely due to the drying occurring during August. DJF has the smallest moistening, while other seasons have peaks of moistening at different levels (3, 4, and 5 km for SON, JJA, and MAM, respectively).

The seasonally averaged zonal and meridional components of horizontal wind are shown in Fig. 3. Westerly wind dominates through four seasons with peaks around 11 and 12 km (Fig. 3a). DJF has the strongest vertical wind shear (35 m s^{-1} over 12 km), while JJA has the weakest shear (10 m s^{-1} over 12 km). The profiles of meridional wind (Fig. 3b) indicate southerly peaks around 0.5 and 0.8 km through four seasons. Northerly wind prevails in DJF, while southerly wind is dominant in SON. The strongest vertical shear of meridional wind occurs between 1 and 4 km in JJA. Figure 4 illustrates the year-long evolution of daily observed surface sensible and latent heat fluxes. DJF has the smallest sensible and latent fluxes of about 20 W m^{-2}. Latent fluxes reach the maximum in JJA with a mean of 104 W m^{-2}, which is more than double the sensible fluxes in JJA (47 W m^{-2}).

The CRM simulation uses a 2D east–west domain that is 600 km long by 40 km deep. The horizontal grid size is 3 km. A stretched grid of 52 levels in the vertical with 100 m at the surface, 550–850 m between 5 and 12
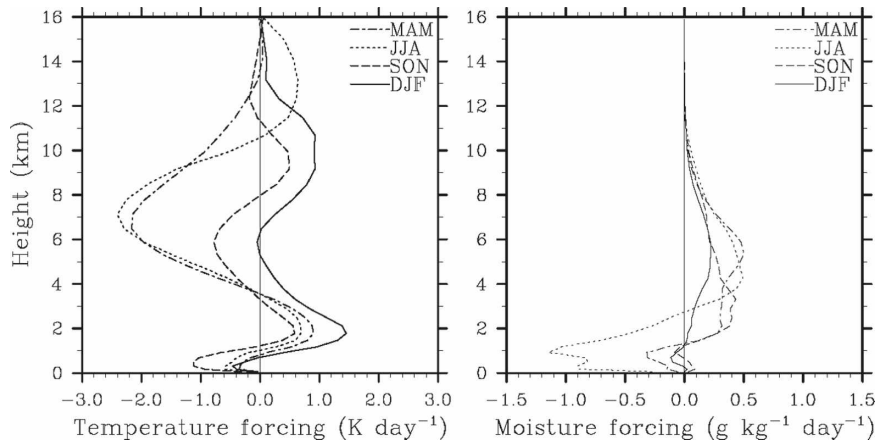
FIG. 2. Vertical profiles of (left) temperature and (right) moisture forcing over the ARM SGP for four seasons (MAM, JJA, SON, and DJF) during year 2000.

km, and 1500 m at the model top is used, and the time step is 15 s. Periodic lateral boundary conditions, and free-slip bottom and top boundary conditions, are applied together with a gravity wave absorber located between 16 km and the model top. The year-long simulation is forced by the evolving temperature and moisture forcing, which is kept constant for an hour around the observed time. The domain-averaged wind at each time step is relaxed using a 2-h time scale to the observed wind, and the observed surface sensible and latent heat fluxes are prescribed in the simulation. The observed wind and surface heat fluxes are interpolated into each model time step. The observed evolving surface temperature is used to calculate the surface upward longwave radiative flux. The surface albedo for direct and diffuse incident solar radiation is set to 0.05 and 0.25 for two spectral intervals (0.2–0.7 and 0.7–5.0 μm), respectively. The radiative fluxes and heating rate

are computed every 300 s and applied at intermediate times. Random perturbations are added to the temperature (0.1 K) and moisture (0.1 g kg^{-1}) fields across the 2D domain (vanishing when averaged over the domain) within the boundary layer every 15 min for the convection initiation.

3. Seasonal variation of CRM-simulated cloud systems

The CRM is integrated continuously with the large-scale forcing described in the last section. For the first time, year-long cloud and radiative properties are produced by a CRM over the ARM SGP site with evolving thermodynamic and dynamic conditions. The statistical analysis of these properties and the evaluation against available observations will help understand the characteristics and radiative effects of cloud systems, and pro-
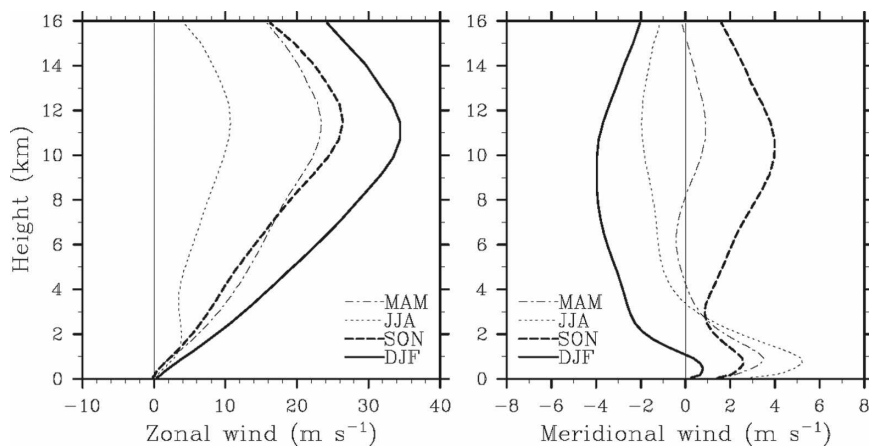
FIG. 3. Vertical profiles of (left) zonal and (right) meridional wind over the ARM SGP for the four seasons during year 2000.
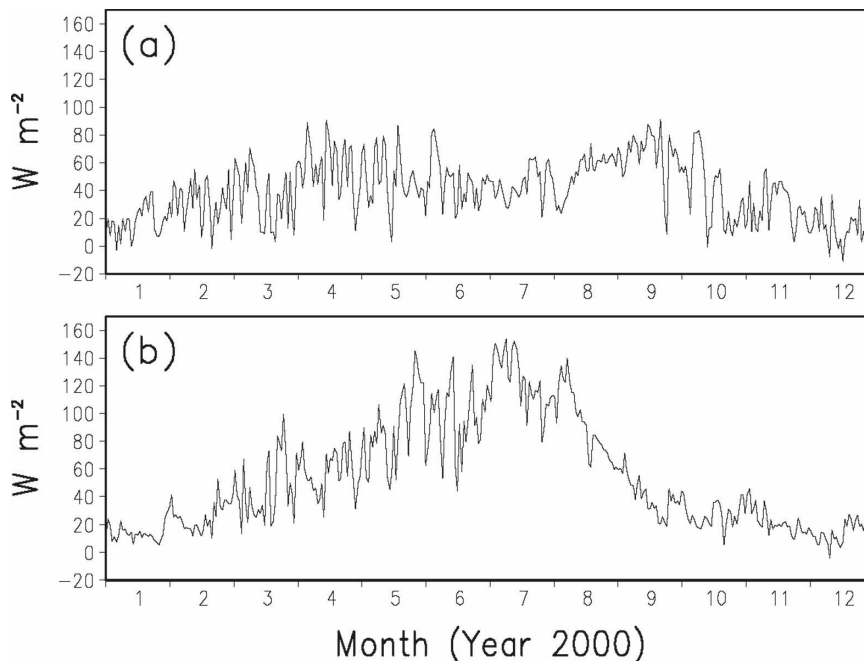
FIG. 4. Year-long evolution of daily surface (a) sensible and (b) latent heat fluxes over the ARM SGP.

vide long-term cloud datasets for improving the parameterization of convection and clouds and GCM simulations. As a standard procedure, the year-long profiles of temperature and moisture differences between the CRM and observations are examined. The biases are similar in magnitude to the TOGA COARE and ARM 1997 IOP simulations (e.g., Wu et al. 1999, 2007c), which have been attributed to various factors including the uncertainties in the model microphysics and the lack of large-scale advection of condensates (e.g., Grabowski et al. 1996; Wu et al. 2000). Since temperature and moisture biases contribute uncertainties to the simulation of cloud and radiative properties and the uncertainties also exist in the retrieved properties, the year-long simulation allows a more comprehensive comparison between CRMs and observations in terms of the magnitude as well as the evolution.

a. Precipitation

The year-long evolution of daily averaged surface rainfall simulated by the CRM is shown in Fig. 5 together with the observed rainfall. The simulated precipitation is in agreement with observations with differences less than 0.4 mm h^{-1}. The correlation coefficient and root-mean-square error (RMSE) between the CRM and observed daily precipitation are 0.97 and 0.06 mm h^{-1} for the entire year, respectively. The mean and standard deviation of daily precipitation are 0.114

and 0.240 mm h^{-1} for the CRM compared to 0.111 and 0.252 mm h^{-1} for the observations, respectively. The observed seasonal variation of precipitation is also well reproduced by the CRM. The spring (MAM) has the largest mean precipitation ($\sim$0.15 mm h^{-1}) followed by the summer ($\sim$0.14 mm h^{-1}) and fall ($\sim$0.12 mm h^{-1}). The winter (DJF) has the smallest rain ($\sim$0.05 mm h^{-1}) for both CRM and observations. Note that the observed precipitation was used in the variational analysis to constrain the large-scale forcing (Xie et al. 2004), which mostly contributes to the successful CRM simulation.

Table 1 lists the correlations between the CRM-produced precipitation and the large-scale temperature and moisture forcing, as well as the surface sensible and latent heat fluxes, respectively. For the entire year, the large-scale advective temperature and moisture forcing have much larger correlations with the precipitation than the surface heat fluxes. When looking at the four seasons, the correlations between the precipitation and large-scale forcing are larger than 0.7 for spring, summer, and fall, but smaller than 0.5 for winter. The precipitation has similar correlations with the large-scale forcing and surface heat fluxes during winter. During summer, the precipitation has the highest correlation (0.98) with the large-scale temperature forcing and the lowest correlations (0.17 and 0.11) with the surface sensible and latent heat fluxes. This suggests that the large-
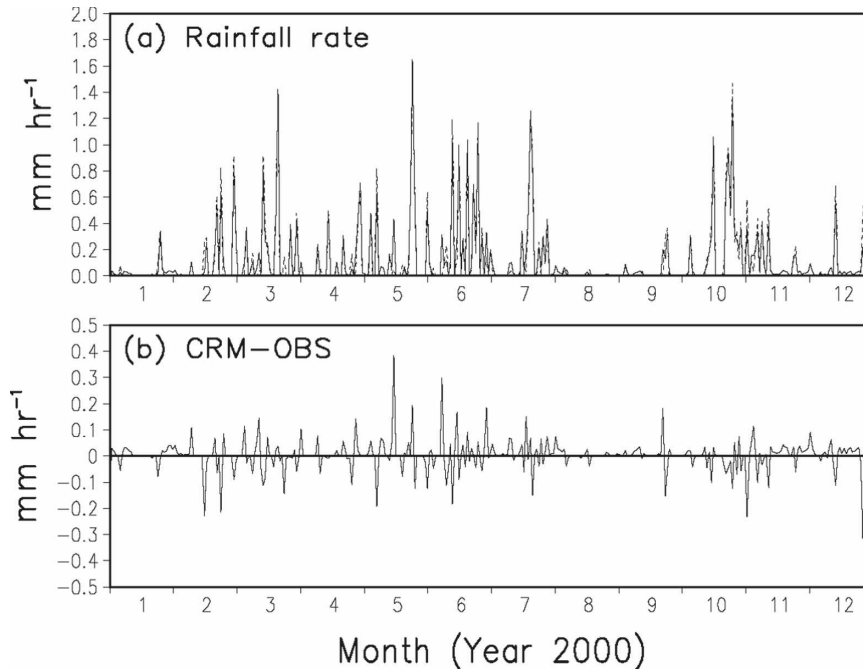
FIG. 5. Year-long evolution of daily surface rainfall rates from (a) CRM (solid) and observations (OBS, dashed), and (b) their differences over the ARM SGP.

scale forcing is the dominant factor for producing the precipitation in summer, spring, and fall, but the surface heat fluxes play a more important role during winter when the large-scale forcing is weak.

Further comparison of hourly surface rainfall between the CRM and observations shows a prominent diurnal variation over the SGP site for the four seasons in Fig. 6. In summer and winter, the composed diurnal variation exhibits an early morning maximum rain-

TABLE 1. Correlation coefficients between daily mean surface rainfall rate, LWP, IWP, and vertically integrated temperature, moisture forcing, and surface sensible (SH) and latent (LH) heat fluxes during year 2000.

	Correlation coefficient				
Variables	ANN	MAM	JJA	SON	DJF
Rain vs T forcing	0.86	0.85	0.98	0.85	0.40
Rain vs q forcing	0.72	0.73	0.68	0.79	0.36
Rain vs SH	0.20	0.37	0.17	0.46	0.22
Rain vs LH	0.05	0.12	0.11	0.15	0.20
LWP vs T forcing	0.51	0.54	0.70	0.59	0.32
LWP vs q forcing	0.58	0.48	0.68	0.66	0.47
LWP vs SH	0.32	0.43	0.33	0.59	0.35
LWP vs LH	0.10	0.26	0.20	0.28	0.02
IWP vs T forcing	0.77	0.83	0.95	0.80	0.22
IWP vs q forcing	0.74	0.79	0.74	0.81	0.60
IWP vs SH	0.24	0.43	0.25	0.52	0.27
IWP vs LH	0.02	0.20	0.16	0.18	0.06

fall and an afternoon minimum. Both the CRM and observations have similar amplitude and peak of rainfall. In spring and fall, the maximum rainfall appears around midnight and the minimum at noon and in early afternoon. The CRM also produces a secondary peak in the morning, which was not shown in observations.

b. Cloud properties

The general agreement between the CRM-simulated and observed year-long precipitation prompts the examination of characteristics of associated cloud systems against limited observations. It is well known that the representation of cloud systems and their radiative effects such as the vertical overlap and horizontal inhomogeneity of clouds (e.g., Geleyn and Hollingsworth 1979; Stephens 1984; Cahalan et al. 1994; Liang and Wang 1997) are two of the major uncertainties in GCMs partly due to the lack of global observations of cloud liquid, ice water condensates, and radiative heating profiles. The year-long CRM simulations will provide unique cloud properties, such as cloud ice and liquid water mixing ratio, and their horizontal and vertical distributions to alleviate the problem.

Figure 7 compares the daily domain-averaged cloud liquid water paths (LWPs) from the CRM with observations retrieved from the ground-based microwave radiometer at the ARM SGP. The observed liquid water paths are averaged over five stations within the SGP.
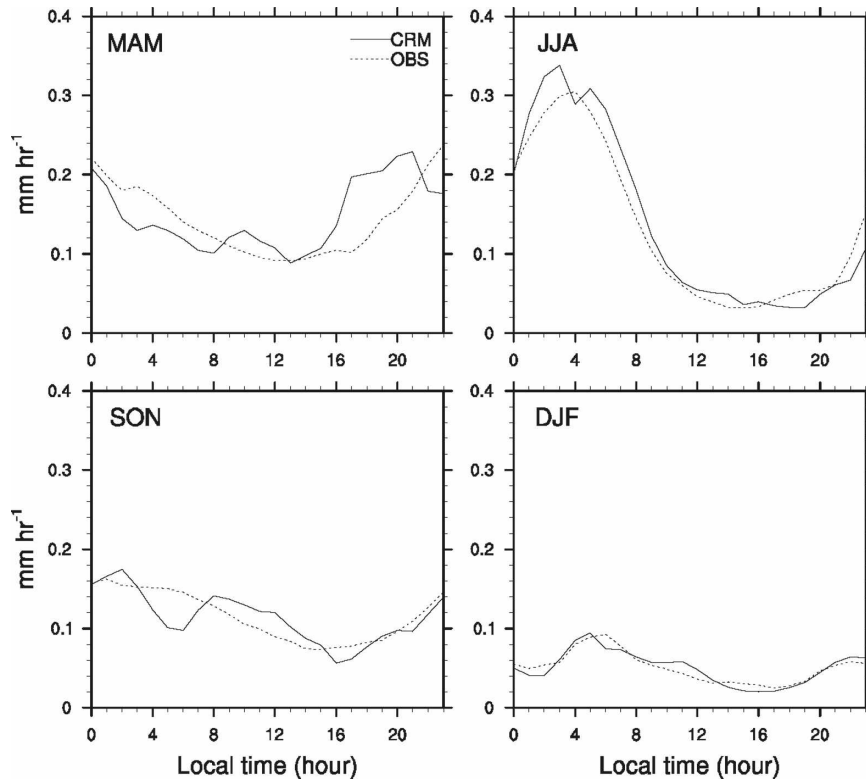
FIG. 6. Composite diurnal variation of hourly surface rainfall rates from CRM and observations (OBS) over the ARM SGP for the four seasons.

The year-long evolution of cloud liquid water simulated by the CRM is in general agreement with that estimated from the point measurement over the SGP site (Fig. 7a). The differences between them are smaller than 0.2 kg m^{-2} during most of the year except for a few days in December when the difference is close to 0.4 kg m^{-2} (Fig. 7b). The correlation coefficient and RMSE between the CRM and observed LWP are 0.729 and 0.056 kg m^{-2} for the entire year, respectively. The annual means (standard deviation) of daily cloud liquid water paths are 0.046 kg (0.071 kg) and 0.055 kg m^{-2} (0.078 kg m^{-2}) for the CRM and observations, respectively. The CRM-produced daily ice water paths (IWPs) shown in Fig. 7c are larger than the liquid water paths (Fig. 7a) during most times of the year. The annual mean and standard deviation of ice water paths are 0.069 and 0.117 kg m^{-2}, respectively, which are 50% more than those of liquid water paths. The dominance of ice water over liquid water is further identified from the vertical profiles of cloud liquid and ice mixing ratio for the three seasons (MAM, JJA, and DJF; Fig. 8). During SON, ice water and liquid water are comparable. The vertical distributions of ice and liquid water vary as seasons change. During summer, the base of ice water is highest at about 3 km, while during winter it is

near the surface. The liquid water has the peak at 3.5 km in summer and near the surface in winter. Graupel and rainwater mixing ratios also undergo a seasonal variation but have smaller magnitudes compared to liquid and ice.

The Geostationary Operational Environmental Satellite (*GOES-8*) retrievals (Minnis et al. 1995, 2002) provide daytime IWP as well as LWP for the comparison with CRM simulations. *GOES-8* LWP and IWP are half-hourly data with 0.5° horizontal resolution, and the daily means over the domain of 35.25–38.25°N and 95.75–99.25°W are compared with those from the CRM (Fig. 9). Overall, CRM and GOES show similar evolutions of LWP and IWP with the correlation coefficient of 0.797 for IWP and 0.588 for LWP. It is noted that the CRM-produced LWP correlates better with the ground-based measurement (0.729) than satellite retrievals (0.588). GOES daytime retrievals show IWP is 68% larger than LWP, but the annual means of IWP and LWP are 0.163 and 0.097 kg m^{-2}, respectively, which are larger than CRMs. Min et al. (2004b) demonstrated that GOES retrievals overestimate cirrus optical depths when compared to multifilter rotating shadowband radiometer (MFRSR) data possibly because of cloud inhomogeneity, mismatches in observed clouds,
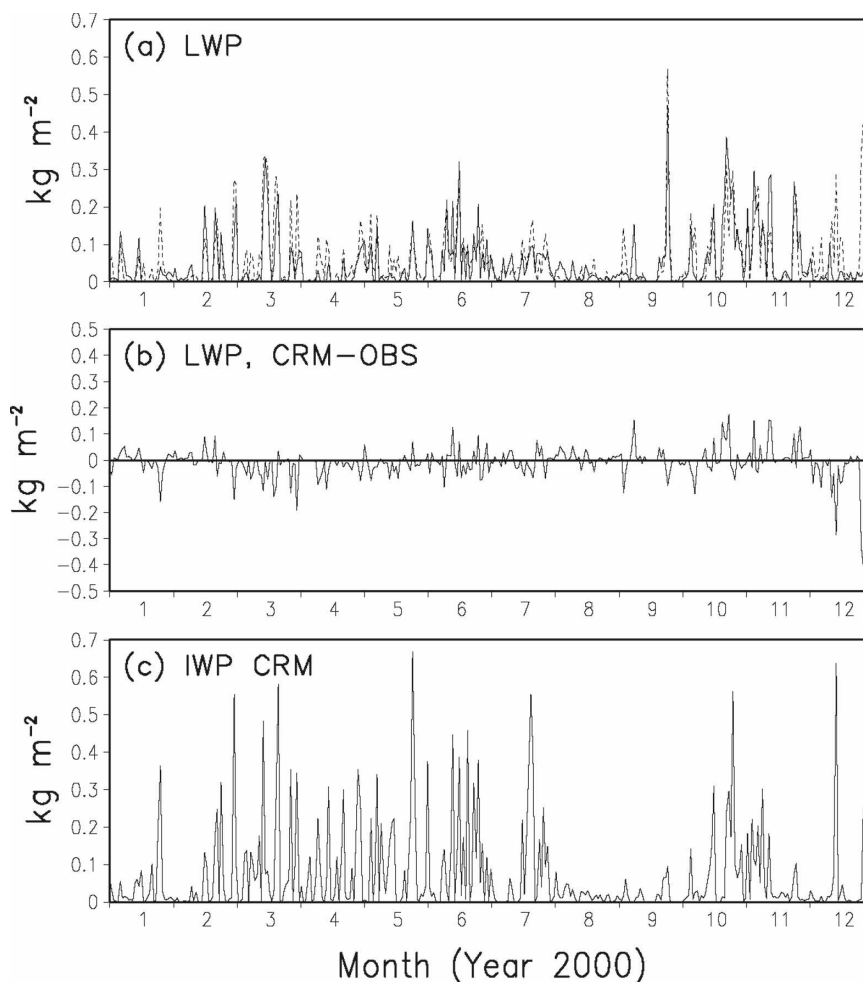
FIG. 7. Year-long evolution of (a) daily cloud LWP from CRM (solid) and the ground-based microwave radiometer retrievals (OBS, dashed), (b) differences between CRM and OBS, and (c) daily cloud IWP from CRM.

and errors in the surface albedo and the ice crystal scattering phase function.

Month-long ice water data retrieved by combining ground cloud radar and satellite high-frequency microwave measurements near the ARM SGP during March 2000 IOP (Seo and Liu 2005) are available for the qualitative check. The temporal resolution of retrieved ice water paths is twice daily. The horizontal grid size is about 20 km over the SGP. The retrieved IWP is averaged over the domain of 35°–38°N and 95°–99°W and superposed over the CRM-produced IWP in Fig. 10. These two independently obtained ice water paths show a similar evolution. Both CRM and retrieved IWPs match well for most events with larger IWPs except one on March 29. It is likely that the 12-h time interval of the retrieved data just missed the peak of the event this day.

Another qualitative comparison can be made by de-riving the cloud optical depths from the CRM-produced liquid and ice water paths and using year-long MFRSR measurements (available during the daytime) at the central facility of SGP. The cloud optical depths from MFRSR are retrieved using algorithms developed by Min and Harrison (1996) and Min et al. (2004a). These products have been validated extensively at the ARM SGP site (Min et al. 2003, 2004b). The original 20-s data are averaged between the LT of 8 a.m. and 4 p.m. to obtain a daily mean. There are 20 days with no data during year 2000. The CRM cloud optical depth is the summation of cloud liquid optical depth (τ_l) and cloud ice optical depth (τ_i), which are calculated using the following formulas (e.g., Stephens 1978; Heymsfield et al. 2003):

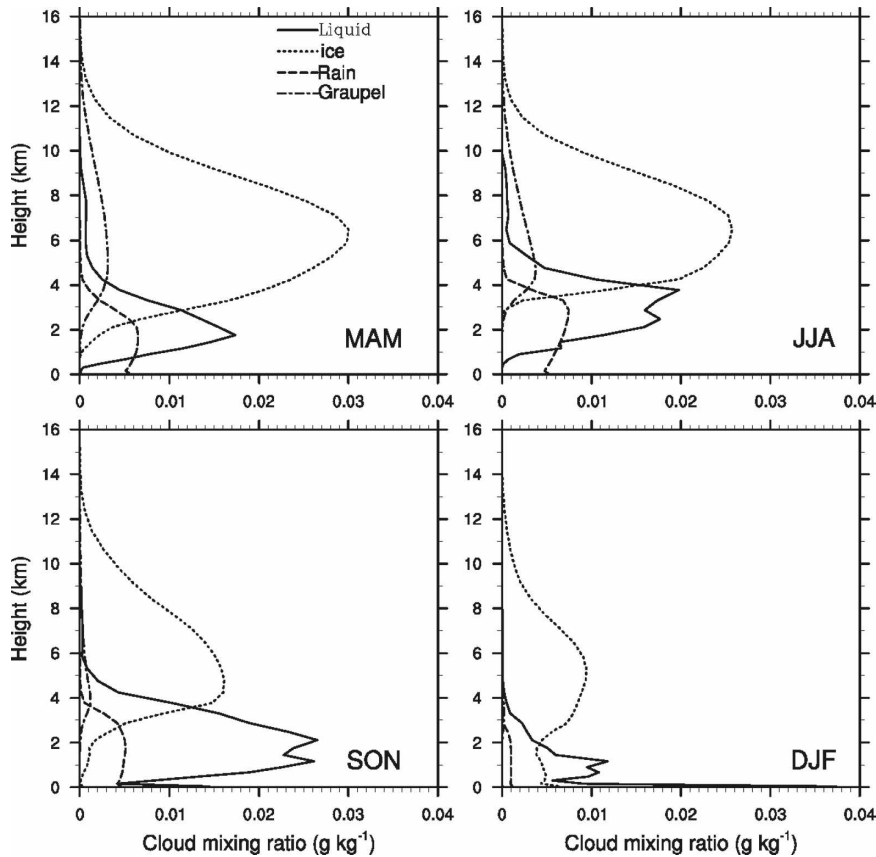$$\tau_l = \frac{3}{2} \frac{\text{LWP}}{r_l}$$

FIG. 8. Seasonal mean vertical profiles of domain-averaged cloud liquid (solid), ice (dotted), graupel (dotted–dashed), and rain (dashed) water mixing ratio from CRM.

and

$$\tau_i = g_0 \text{IWP}\left[1 + \left(\frac{g_1}{g_0}\right)\frac{1}{r_i}\right].$$

LWP and IWP are the liquid and ice water paths (in g m^{-2}), g_0 and g_1 are 0.01256 and 0.725, r_l and r_i are the effective radii of liquid and ice water (in μm), with 10 and 30 μm being used for r_l and r_i, respectively. The CRM-produced cloud optical depths are averaged during the daytime between 8 a.m. and 4 p.m. As shown in Fig. 11, CRM and MFRSR cloud optical depths share the similar evolution during the year. The correlation coefficient and RMSE between the CRM and observed optical depths are 0.64 and 17.67 for the entire year, respectively. Despite the variation of differences between modeled and retrieved daily optical depths, the annual means are close with 9.7 and 11.6 for the CRM and MFRSR, respectively. This is expected when comparing the model outputs with the point measurements. The overall agreement does provide some confidences for the CRM cloud products and the performance of microphysical parameterization scheme. Besides the

above two ice-related datasets, Mace et al. (2006) retrieved multiyear cloud ice and liquid water from continuous ground-based remote sensing measurements (MFRSR was used for validation). However, this dataset is limited for overcast uniform skies, which is also the case for the continuous baseline microphysical retrieval (MICROBASE) cloud liquid and ice water properties (M. Miller 2007, personal communication).

Cloud fractions are calculated using a threshold of 0.2 g m^{-2} of column integrated cloud liquid and ice water paths for the CRM simulations following Wu and Moncrieff (2001). The evolution of cloud fractions from the CRM (Fig. 12a) is in general agreement with the International Satellite Cloud Climatology Project (IS-CCP) satellite retrievals averaged over the SGP (Zhang et al. 2004). ISCCP is 3-hourly data with 2.5° resolution, and the daily means over the domain of 35°–37.5°N and 95°–100°W are used for the comparison. The year-long mean of 0.670 from the CRM is slightly larger than 0.585 from ISCCP. However, differences between the two estimations are larger in daily means (Fig. 12b), which could be due to the uncertainties in the satellite
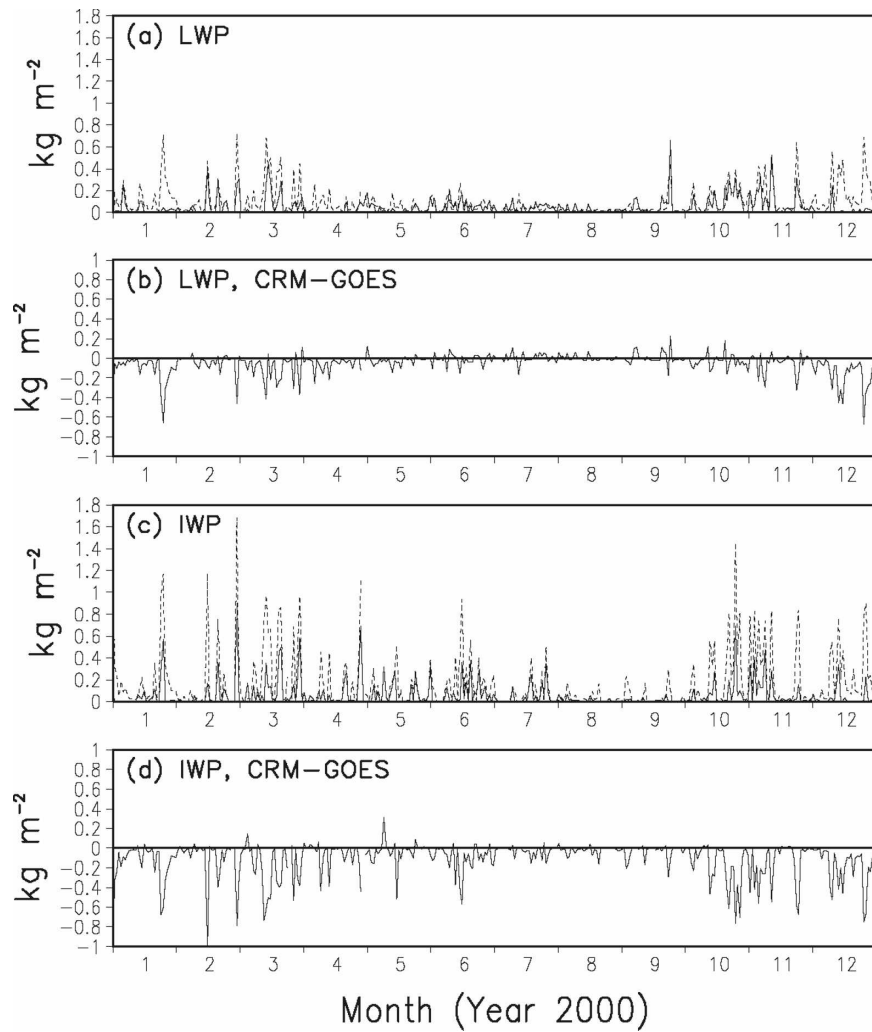
FIG. 9. Year-long evolution of (a) daily averaged daytime cloud LWP from CRM (solid) and *GOES-8* (dashed) and (b) the differences, and (c) daily averaged daytime cloud IWP from CRM (solid) and *GOES-8* (dashed) and (d) the differences.
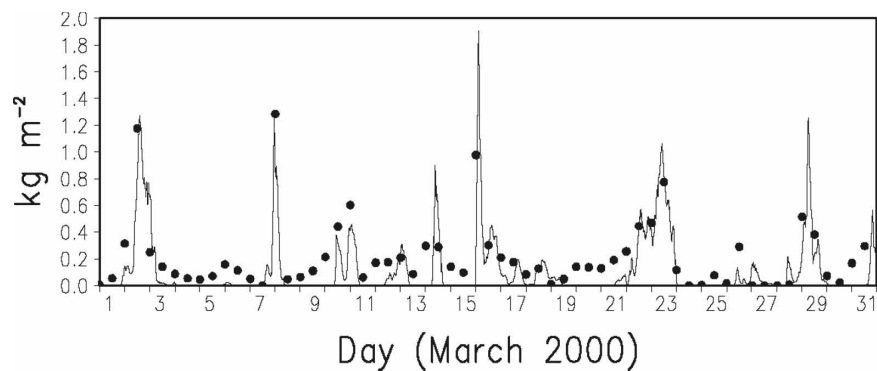

FIG. 10. Month-long (1–31 Mar 2000) evolution of cloud ice water paths from 15-min CRM outputs (solid line) and twice per day satellite retrievals (dots; see text for details).
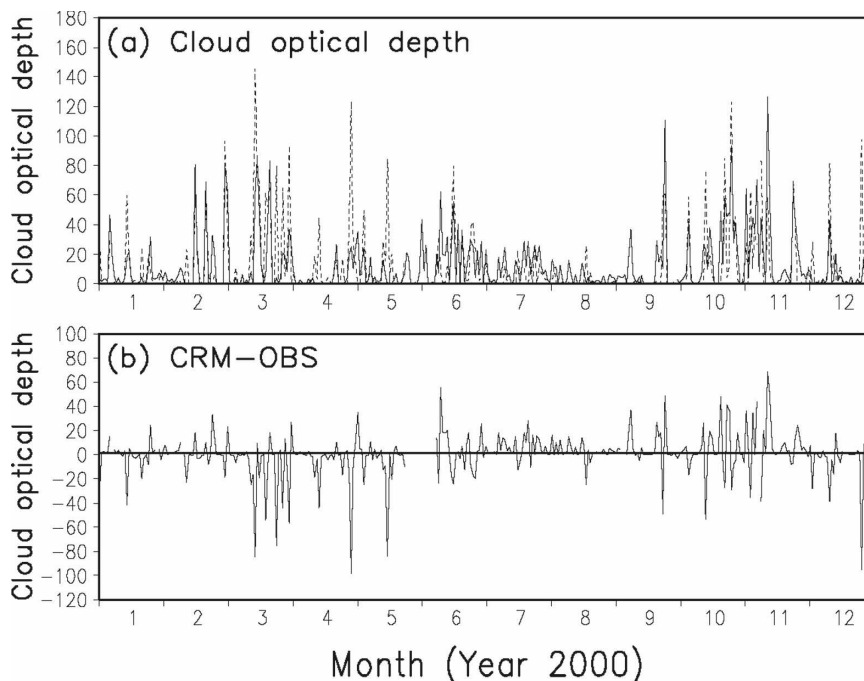
FIG. 11. Year-long evolution of (a) daily cloud (liquid and ice) optical depths from CRM (solid) and MFRSR (dashed, see text for details), and (b) differences between CRM and radar retrievals.

retrievals and the sensitivity of CRM cloud fraction to the thresholds. When the ISCCP cloud fraction is compared with that from *GOES-8* retrievals (Minnis et al. 1995, 2002), the former is larger than the latter (Fig. 12c). The year-long average from GOES is 0.428, which is smaller than ISCCP. The correlation coefficient between the CRM and GOES is 0.560, which is larger than 0.361 between the CRM and ISCCP cloud fraction. When the thresholds change from 0.2, 2 to 20 g m^{-2}, the year-long mean cloud fractions from the CRM vary from 0.670, 0.504 to 0.342.

The vertical profile of cloud fraction from the CRM is further evaluated with the derived cloud fraction from the Active Remotely Sensed Clouds Locations (ARSCL) cloud-base and cloud-top height data (Clothiaux et al. 2000). Following the approach of Yang et al. (2006) and Lazarus et al. (2000), the vertical profile of ARSCL hourly cloud fraction is computed using the same vertical resolution as the CRM. The diurnal variation of the cloud fraction profile is compared between CRM and ARSCL for the four seasons (Fig. 13). Both products show similar diurnal variation of cloud fraction in the upper and middle levels with higher cloud amount at night than in the daytime. However, the peak of cloud amount from CRM is at about 7 km, which is 2 km lower than that from ARSCL. The CRM has a larger cloud amount

than ARSCL in the middle levels, which is dependent of the use of thresholds. The largest difference between the two products is in the low-level cloud amount. ARSCL has more shallow clouds in the daytime than at night during all seasons with a maximum between 8 LST and noon. CRM shows much smaller shallow cloud amount than ARSCL especially during MAM and JJA. During SON, there is a small peak of shallow clouds at noon. The underproduction of shallow cloud amount in CRM could be due to the use of coarse horizontal resolution.

The year-long CRM simulation allows a robust analysis of frequency distribution of LWP and IWP for the first time. Figures 14 and 15 present frequency histograms of LWP and IWP using the 15-min CRM outputs for the four seasons, respectively. Three categories of LWP are clearly present in a nonsymmetrical and skewed distribution, that is the large size of 100–1000 g m^{-2}, the medium size of 10–100 g m^{-2}, and the small size of 1–10 g m^{-2}. The winter season has lower occurrences of large liquid water paths than the other three seasons. For the medium size of liquid water, the distribution is more skewed in winter than in the other seasons, and the liquid water path of 10–20 g m^{-2} reaches 20% in winter and about 10% in the other seasons. The frequency of small size of liquid water paths has the skewed distribution in spring, summer,
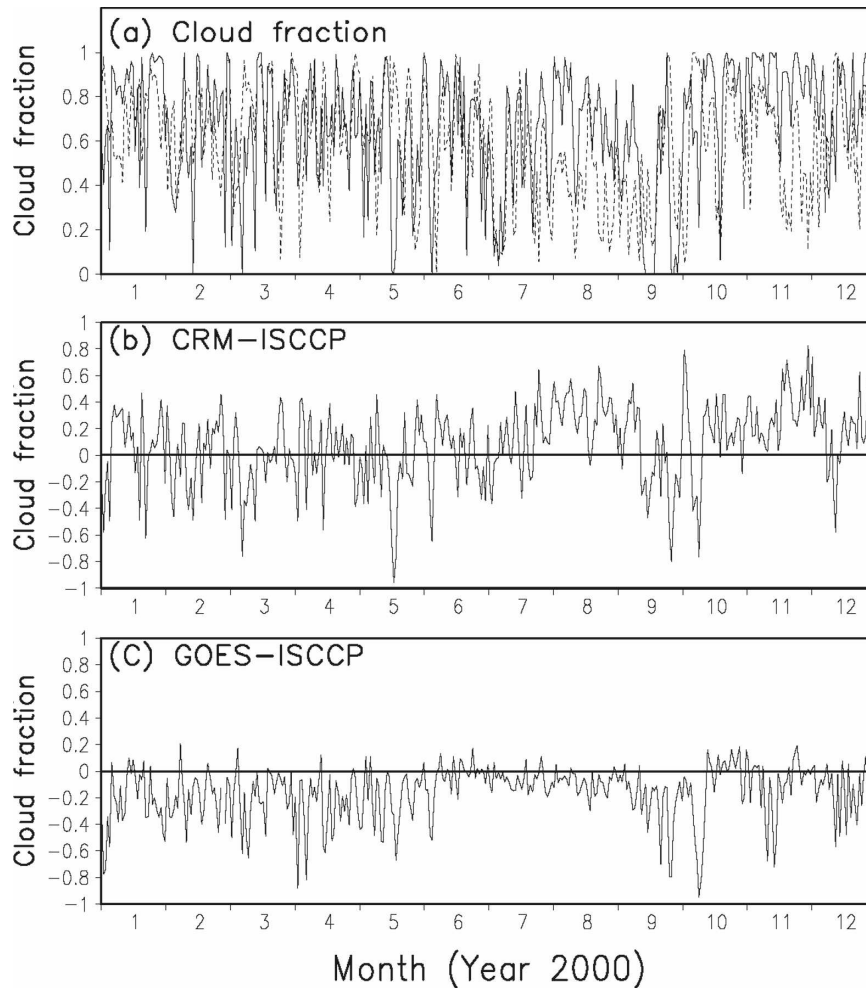
FIG. 12. Year-long evolution of (a) daily cloud fraction from CRM (solid) and ISCCP (dashed), (b) differences between CRM and ISCCP, and (c) differences between ISCCP and GOES.

and winter, but relatively flat distribution in fall. The ice water paths also exhibit skewed distributions for three categories. Winter, again, has lower occurrences of large ice water but more frequent occurrences of small ice water than the other three seasons, which may be explained by less moisture and colder temperature in winter.

The correlation between the year-long LWP and IWP, and the large-scale forcing and surface heat fluxes are calculated and listed in Table 1. For the entire year, the IWP has higher correlation with the large-scale temperature and moisture forcing than the LWP (0.77 and 0.74 versus 0.51 and 0.58, respectively). The correlations between LWP and surface sensible and latent heat fluxes (0.32 and 0.10) are higher than those between IWP and the surface fluxes (0.24 and 0.02). The ice water is largely produced above the freezing level

within deep convection, which responds to the large-scale forcing while the liquid water can be affected by both the large-scale forcing and surface heat fluxes. Therefore, the correlations between the IWP and the forcing are higher than those between the IWP and the surface fluxes, while the correlations are similar for the LWP. Spring, summer, and fall show similar correlations. But in winter, since the forcing is weak, the surface sensible heat flux is as important as the forcing in producing clouds.

The year-long CRM simulation also provides cloud mass fluxes, which are crucial for the determination of convective heating and moistening in convection parameterization schemes of GCMs but are not available from the measurement. Following Grabowski et al. (1996), updraft and downdraft mass fluxes are obtained in regions where the total condensate (liquid, ice, grau-
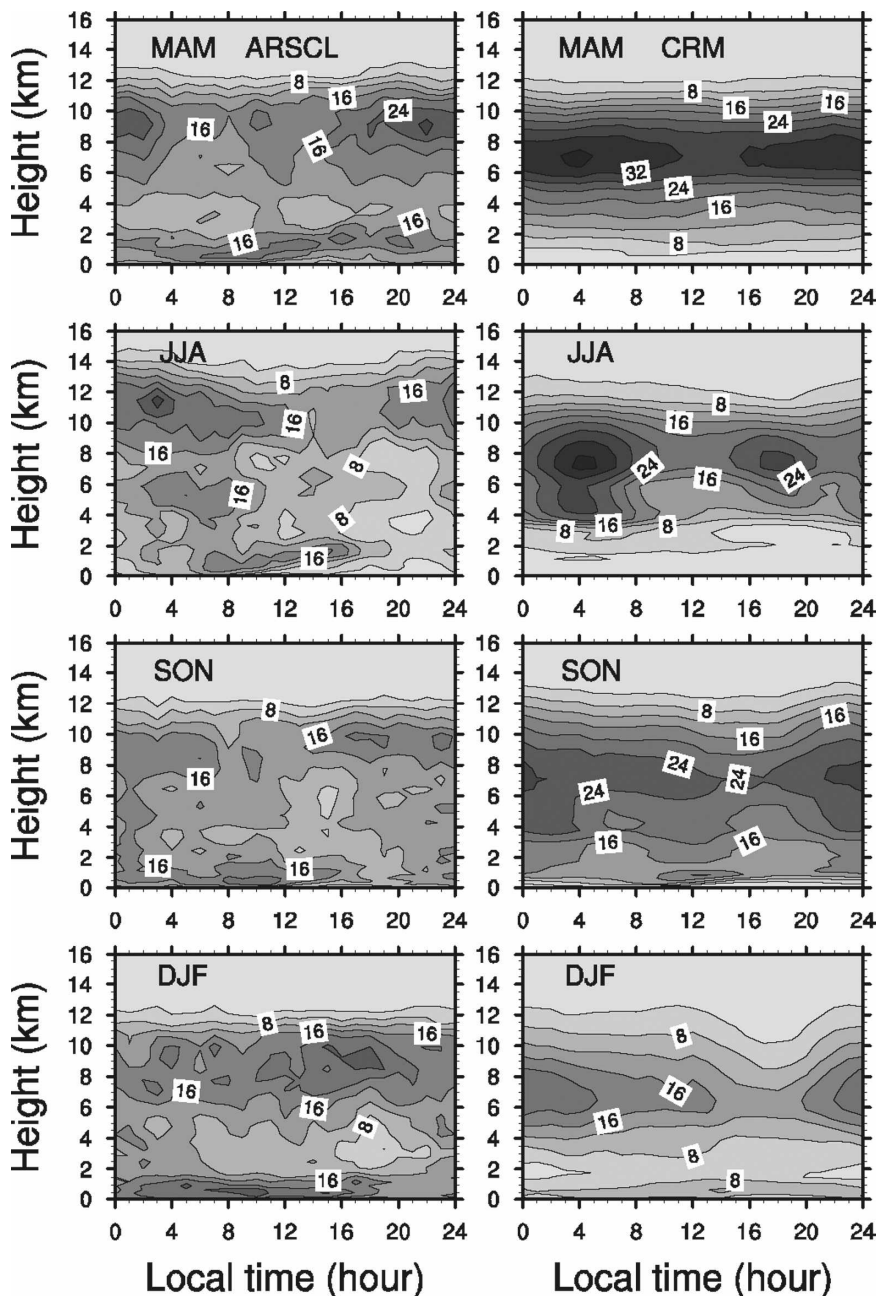
FIG. 13. Composite diurnal variation of hourly profile of cloud fraction (%, contour interval is 4%) from (left) ARSCL and (right) CRM over the ARM SGP for the four seasons.

pel, and rain) mixing ratio is equal to or larger than 0.1 g kg^{-1} at a given level. The vertical distribution of cloud mass fluxes shows a large seasonal variation (Fig. 16). Spring and summer have the strongest total cloud mass flux, while winter has the weakest. Peaks of total flux decrease from 7 km in spring to 6 km in summer to 4 km in fall, which is largely due to the variation of peaks of updraft mass fluxes. The downdraft has peaks around 2–4 km with the highest in summer and is an

equally important component as the updraft in midlatitude cloud systems.

c. Radiative properties

Analysis of the seasonal variation of CRM-simulated cloud systems together with available observed cloud properties provide useful insights into the performance of the CRM over land. Further validation can be conducted by comparing the CRM-produced cloud radia-
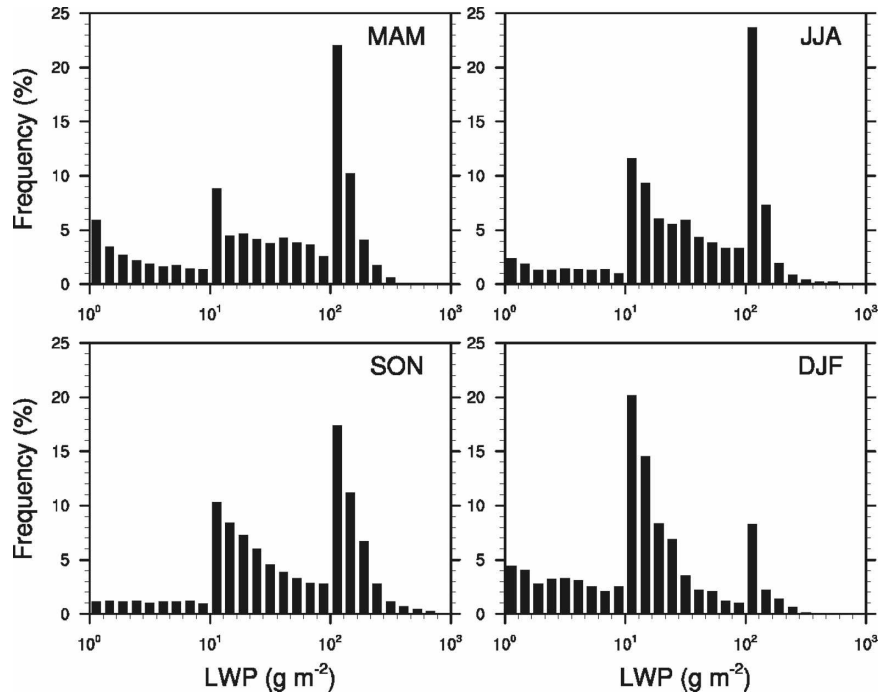
FIG. 14. Frequency histograms of cloud LWP from 15-min CRM outputs for four seasons. The widths of the size bins are 100, 10, and 1 g m^{-2} for three categories of LWP, i.e., large size of 100–1000 g m^{-2}, medium size of 10–100 g m^{-2}, and small size of 1–10 g m^{-2}, respectively.
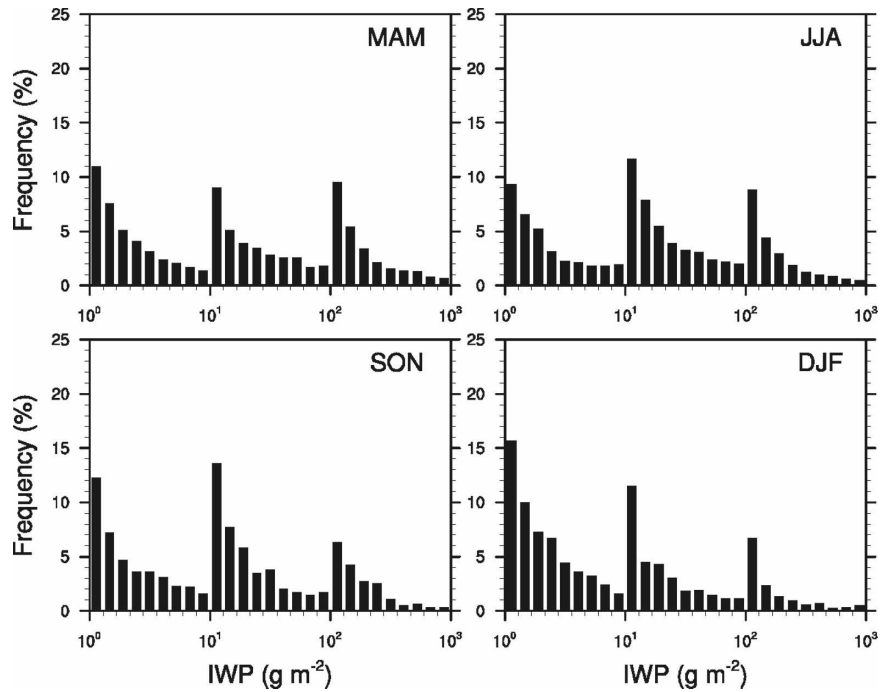

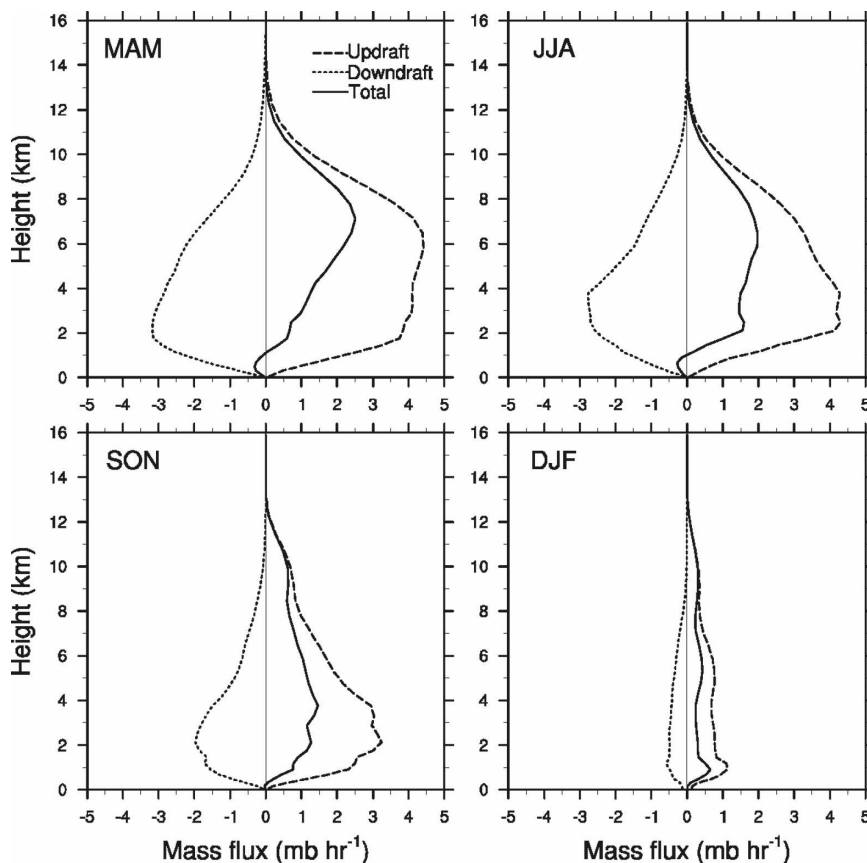FIG. 15. Same as Fig. 14, but for IWP.

FIG. 16. Seasonal mean vertical profiles of updraft (dashed), downdraft (dotted), and total cloud mass fluxes (solid) from CRM.

tive properties with satellite- and surface-measured radiative fluxes. Since the surface albedo over land varies as the seasons change, it will be interesting to find out if and how the use of constant surface albedo in the CRM will affect the simulation of radiative fluxes, which can provide useful guidance for further improvement of CRM simulations.

Table 2 lists means and standard deviations of net longwave (LW) and shortwave (SW) radiative fluxes at TOA, the surface for the entire year, and the four seasons from the CRM and observations. The net flux is defined as the downward flux minus upward flux. The observed TOA longwave and shortwave fluxes are derived from *GOES-8* (Minnis et al. 1995), and the observed surface longwave and shortwave radiative fluxes are obtained using data measured from 22 solar infrared stations in the SGP. The CRM-produced annual mean LW is close to the observed LW at TOA and the surface with the difference of less than 6 W m^{-2}. For the seasonal means, the differences of LW between the CRM and observations are within 10 W m^{-2}. The differences of the annual mean TOA SW between the

CRM and observations are less than 2 W m^{-2}. But the differences of the annual mean surface SW between the CRM and observations are 18 W m^{-2}. Both the CRM and observations have similar standard deviations of daily mean TOA, and surface LW and SW for the year, and for the four seasons. The use of constant surface albedo in the CRM is likely the factor leading to the difference (more discussion later). The uncertainty in obtaining the area mean surface SW from 22 stations may also be partly responsible for this difference (e.g., Li et al. 2002). It is noted from Table 2 that the seasonal variations of mean surface SW from the CRM are consistent with those from observations. The mean surface SW increases from spring to summer then decreases to fall and winter. The largest differences of 11.8 and 28.4 W m^{-2} are present in TOA and the surface SW, respectively, during spring.

To understand the possible cause for the difference in net radiative fluxes, the downward and upward components of LW and SW from the CRM are compared with observations in Table 3. The LW at TOA has only upward components, which are the same as the net

TABLE 2. Annual (ANN) and seasonal (MAM, JJA, SON, and DJF) means and std dev (SD) of daily net (downward minus upward fluxes) LW and SW at TOA and the surface (SFC) during year 2000.

		TOA									
		LW					SW				
Net radiative fluxes (W m^{-2})		ANN	MAM	JJA	SON	DJF	ANN	MAM	JJA	SON	DJF
Mean	CRM	−240.7	−241.3	−255.0	−240.4	−225.6	238.8	287.9	335.4	187.9	140.4
	OBS	−241.9	−239.0	−262.6	−246.7	−218.6	237.4	276.1	338.9	196.9	133.7
SD	CRM	26.7	26.6	25.8	30.5	18.6	96.2	68.3	34.7	74.5	40.4
	OBS	33.1	31.9	29.9	33.8	18.6	97.9	74.8	42.6	70.8	42.7

		SFC									
		LW					SW				
Net radiative fluxes (W m^{-2})		ANN	MAM	JJA	SON	DJF	ANN	MAM	JJA	SON	DJF
Mean	CRM	−62.2	−66.2	−71.0	−52.0	−59.3	170.0	208.9	240.4	128.5	99.4
	OBS	−56.6	−62.7	−60.4	−52.2	−50.7	152.4	180.5	217.6	126.4	82.7
SD	CRM	31.1	27.6	20.7	37.6	33.3	79.3	66.3	38.2	68.0	39.6
	OBS	25.3	26.0	17.4	28.5	26.1	74.8	73.0	43.8	55.9	39.4

TOA LW in Table 2 but with the positive sign. The slight difference of surface upward LW between the CRM and observations for the year and seasons is due to the uniform surface temperature used in the CRM domain. The CRM downward LW is within 10 W m^{-2} of the observed LW during four seasons and has basically the same annual mean as the observation. For SW, the annual mean downward flux at the surface is about 7 W m^{-2} larger than the observed annual mean while the upward flux is about 11 W m^{-2} smaller than the observation, which leads to more than 18 W m^{-2} difference in net SW at the surface. The ratio (or annual mean surface albedo) of upward over downward fluxes is 0.15 and 0.21 for the CRM and observation, respectively. In the current CRM simulation, the surface albedos of 0.05 and 0.25 are used for two spectral inter-

TABLE 3. ANN and seasonal means and SD of daily LW and SW upward (UP) and downward (DN) radiative fluxes at TOA and the SFC during year 2000.

		TOA									
		SW UP					SW DN				
Radiative fluxes (W m^{-2})		ANN	MAM	JJA	SON	DJF	ANN	MAM	JJA	SON	DJF
Mean	CRM	103.1	116.5	122.6	98.5	73.9	342.0	404.4	458.1	286.4	214.3
	OBS	106.2	130.7	121.0	90.4	81.8	343.6	406.8	459.9	287.2	215.6
SD	CRM	41.8	43.4	38.4	37.2	29.2	106.6	53.5	25.2	63.2	36.3
	OBS	48.3	56.1	48.2	37.7	28.6	107.1	53.6	25.5	63.5	36.7

		SFC									
		LW UP					LW DN				
Radiative fluxes (W m^{-2})		ANN	MAM	JJA	SON	DJF	ANN	MAM	JJA	SON	DJF
Mean	CRM	391.1	395.7	460.1	385.2	321.0	328.9	329.5	389.0	333.2	261.7
	OBS	389.4	393.8	458.2	383.6	319.5	332.8	331.1	397.9	331.4	268.8
SD	CRM	60.9	33.6	22.1	50.8	31.5	57.6	34.1	19.0	47.4	38.2
	OBS	60.7	33.4	21.8	50.7	31.1	59.5	38.1	18.6	55.2	32.5

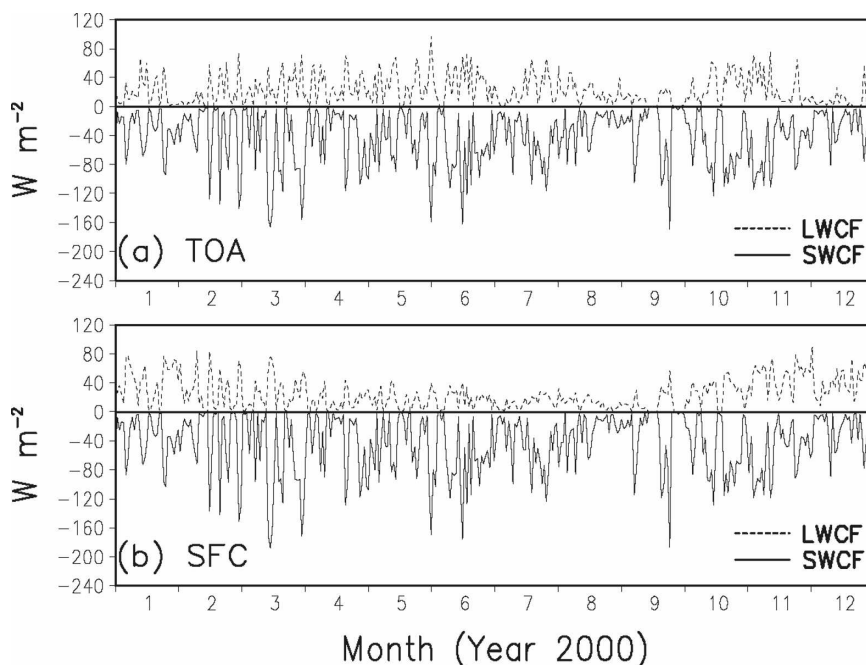|		SFC									
		SW UP					SW DN				
Radiative fluxes (W m^{-2})		ANN	MAM	JJA	SON	DJF	ANN	MAM	JJA	SON	DJF
Mean	CRM	29.7	36.7	41.3	22.5	18.0	199.7	245.5	281.7	151.0	117.5
	OBS	40.5	41.5	53.1	34.5	32.4	192.9	222.0	270.7	160.9	115.2
SD	CRM	13.8	12.0	7.0	12.2	7.4	93.1	78.3	45.2	80.2	47.0
	OBS	17.9	16.2	10.6	19.4	16.5	89.9	88.7	54.1	74.9	45.0

FIG. 17. Year-long evolution of daily SWCF and LWCF at (a) TOA and (b) the surface from CRM.

vals, 0.2–0.7 and 0.7–5.0 μm, respectively, for the entire year, which lead to a smaller mean albedo compared with the observation. The use of constant surface albedo (about 0.15) for the entire year also does not fit well with observations. The observed seasonal mean albedo is 0.19, 0.20, 0.20, and 0.30 for MAM, JJA, SON, and DJF, respectively. The effects of varied surface albedo on the CRM simulation of cloud systems over land will be investigated in another study. The coupling of CRM with a surface model that physically determines the surface albedo should provide the better solution for this problem.

To examine the impact of cloud systems on radiative fluxes, the cloud radiative forcing can be obtained by subtracting the clear-sky radiative fluxes from the total radiative fluxes. Figure 17 shows the year-long evolution of shortwave and longwave cloud radiative forcing (SWCF and LWCF) at TOA, and the surface from the CRM. The SWCF is all negative representing the cooling effects of clouds by blocking the solar radiation, while the LWCF is all positive indicating the warming effects of clouds by reducing the outgoing longwave radiation. The seasonal variations of TOA and surface SWCF are clearly following those of cloud liquid and ice water. The largest SW cloud radiative cooling is in spring and the smallest in winter (Table 4). The LWCF shows different seasonal variations at TOA and the surface. While the largest TOA LW cloud radiative warm-

ing appears in spring, the largest surface LW cloud radiative warming occurs in winter (Table 4). More frequent deep convection in spring and summer and the presence of larger cloud ice and liquid water near the surface in winter (Fig. 8) contribute to the different seasonal variations in TOA and surface longwave cloud forcing.

Table 4 also compares the annual and seasonal mean LWCF and SWCF from CRM with those from ISCCP. The annual means and standard deviation of cloud radiative forcing at both TOA and the surface are similar between CRM and ISCCP, and the difference between them is less than 10 W m^{-2}. But the seasonal mean cloud forcing shows larger differences with the largest (close to 20 W m^{-2}) in spring. The increase of differences with shorter averaging periods can be readily identified in the scatter diagrams of CRM versus ISCCP daily mean cloud radiative forcing (Fig. 18). While the daily means are packed around the diagonal lines, there are days when the differences of daily means between CRM and ISCCP are much larger than annual and seasonal means.

The year-long CRM simulation provides a unique opportunity for examining the seasonal variation of radiative heating, which will be a valuable product for validating and improving GCM simulations. Figure 19 presents the vertical profiles of shortwave, longwave, and total radiative heating rates from the CRM

TABLE 4. ANN and seasonal means and SD of daily LW and SW cloud radiative forcing (all-sky minus clear-sky radiative fluxes) at TOA and the SFC from CRM and ISCCP during year 2000.

Cloud radiative forcing (W m^{-2})		TOA									
		LW					SW				
		ANN	MAM	JJA	SON	DJF	ANN	MAM	JJA	SON	DJF
Mean	CRM	22.1	26.9	25.9	21.0	14.2	−41.8	−46.0	−46.9	−45.0	−29.1
	ISCCP	30.3	37.0	29.2	25.8	29.2	−43.8	−64.5	−44.2	−35.7	−30.4
SD	CRM	20.0	20.4	20.6	19.8	16.6	38.4	44.3	37.2	39.0	28.8
	ISCCP	19.7	23.7	20.1	17.9	14.2	39.3	48.2	40.6	32.7	21.5
Cloud radiative forcing (W m^{-2})		SFC									
		LW					SW				
		ANN	MAM	JJA	SON	DJF	ANN	MAM	JJA	SON	DJF
Mean	CRM	25.1	19.6	14.8	28.9	37.3	−43.7	−48.7	−48.3	−46.7	−30.8
	ISCCP	21.8	26.0	12.1	20.7	28.7	−45.3	−68.4	−45.9	−36.4	−30.0
SD	CRM	21.0	18.2	9.7	22.3	23.9	42.0	49.4	40.4	42.1	31.7
	ISCCP	14.6	14.2	8.5	15.4	13.9	41.8	51.6	42.4	34.2	22.5

for the four seasons. The SW heating undergoes a clear seasonal variation with the largest rate (1 K day^{-1}) in summer and the smallest rate (0.5 K day^{-1}) in winter. The peak of heating is around 7–9 km and slightly lower in winter than in spring, summer, and fall. These peaks are due to the warming above and cooling below clouds (Fig. 8), which are shown by the difference of all-sky and clear-sky SW heating
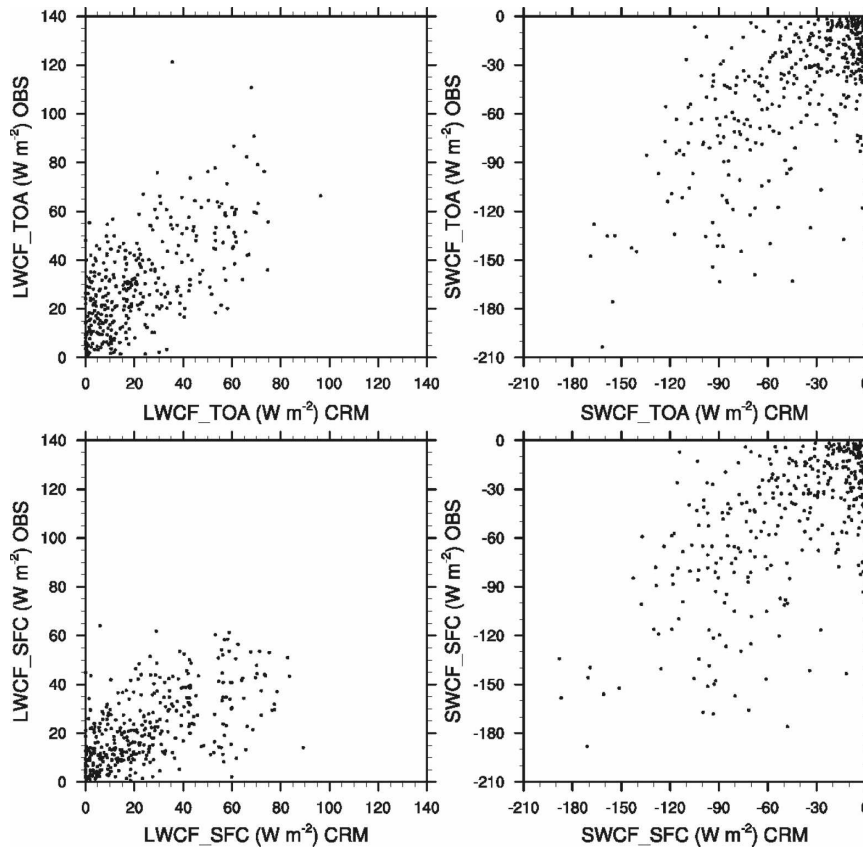

FIG. 18. Scatter diagrams of daily SWCF and LWCF at TOA and the surface from CRM vs ISCCP.
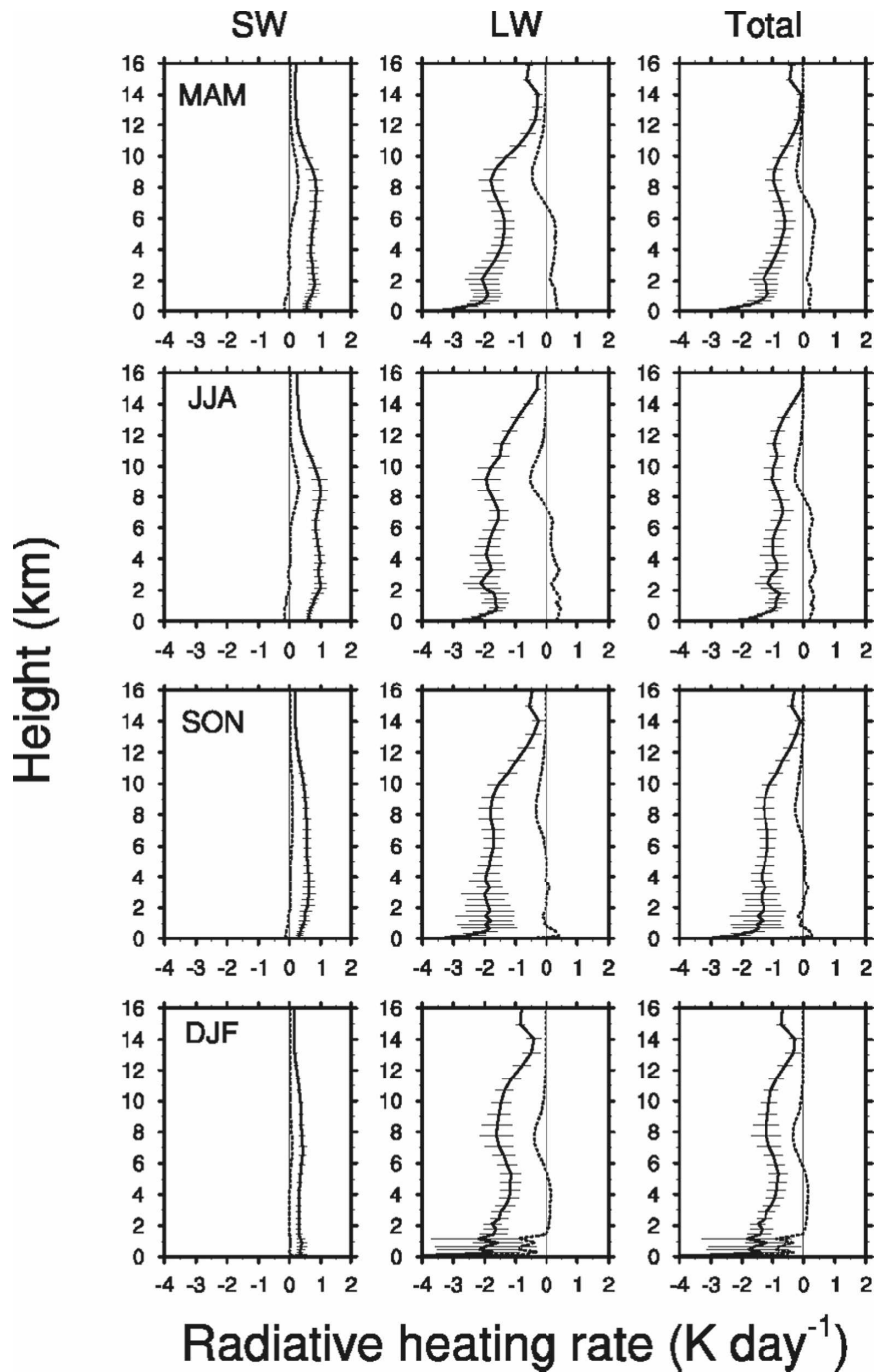
FIG. 19. Seasonal mean vertical profiles of daily all-sky (solid) and cloudy-sky (dotted) (left) SW, (middle) LW, and (right) total (SW + LW) radiative heating rate from CRM. The horizontal bars are the std dev of all-sky heating rates.

profiles (dotted lines in the left panel of Fig. 19). During winter, there is a small cloudy-sky SW heating below 1 km, which is the result of solar heating by lower clouds near the surface. The LW cooling rates through the troposphere are about twice as large as the SW

heating, which leads to similar total and LW cooling profiles. Near the surface, a strong cooling (-4 K day^{-1}) appears for all the seasons and has a large variation (large standard deviation) in winter due to the presence of low-level clouds. The LW also
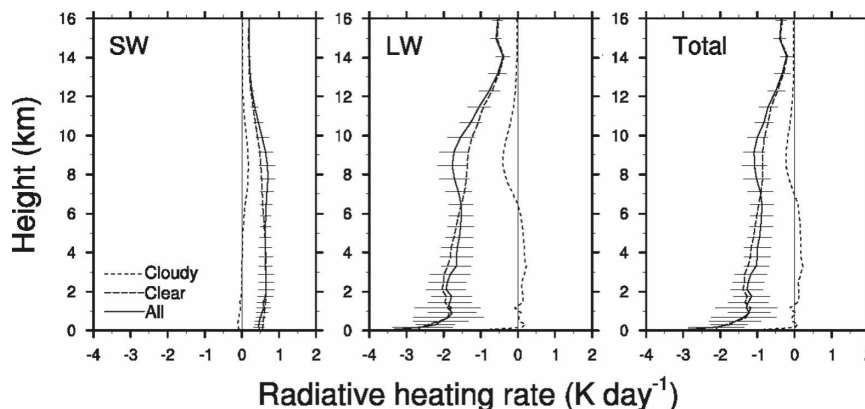
FIG. 20. Annual mean vertical profiles of daily all-sky (solid), clear-sky (dashed), and cloudy-sky (dotted) (left) SW, (middle) LW, and (right) total (SW + LW) radiative heating rate from CRM. The horizontal bars are the std dev of all-sky heating rates.

shows a cooling peak around 8–9 km and is slightly lower in winter than in other seasons. The existence of upper-level clouds results in the cooling above and warming below (dotted lines in the middle panel of Fig. 19) because the flux above clouds is larger than that within clouds. The vertical structure of net cloudy-sky total (LW + SW) heating profiles (dotted lines in the right panel of Fig. 19) is similar to that of cloudy-sky LW heating profiles but with smaller upper-level cooling peaks because of the partial cancellation of SW heating and LW cooling.

The impacts of clouds on the seasonal mean radiative heating profiles are also present in the annual mean profiles (Fig. 20). While the clear-sky SW heating decreases with height above 6 km and tends to destabilize the upper troposphere, the cloudy-sky SW heating with a peak around 9 km tends to stabilize the layer below and destabilize the layer above (left panel of Fig. 20). Opposite features are shown in the LW heating. While the clear-sky LW cooling decreases from 2 km up and tends to stabilize the troposphere, the cloudy-sky LW cooling with a peak around 9 km and LW warming with a peak around 4 km tends to destabilize the layer below 9 km and stabilize the layer above (middle panel of Fig. 20). The cloudy-sky LW cooling also has a peak near the surface, which enhances the clear-sky near surface LW cooling. The cloudy-sky total (LW + SW) radiative heating profile (right panel of Fig. 20) indicates the cooling above 7 km and the heating below, which counterbalances the clear-sky cooling profile between 9 and 4 km. The near surface cloudy-sky total radiative cooling reinforces the large near surface clear-sky cooling. The resulting vertical distribution of all-sky radiative cooling tends to stabilize the layers above 9 and below 4 km but destabilize the layer between.

4. Summary

The lack of global long-term observations of cloud properties, especially cloud ice water, presents a major problem for improving the representation of clouds and cloud–radiation interaction in GCMs. The year-long cloud-resolving simulation provides a potentially powerful approach to generating years-long thermodynamic and dynamic consistent cloud properties over global climate sensitive regions. The variational analysis that constrains the mesoscale model outputs (like NOAA RUC datasets) with the surface and TOA measurements (including precipitation, sensible, latent heat, and radiative fluxes) proves to be an accurate way for deriving the large-scale forcing. As expected, the year-long (3 January–31 December 2000) CRM integration of cloud systems forced by the variationally constrained temperature and moisture advection over the ARM SGP simulates the evolution of daily mean surface precipitation close to observations with a high correlation coefficient of 0.97. The CRM-produced year-long cloud properties compare reasonably well with available observations from ARM. The modeled cloud liquid water path exhibits similar evolution as does the observed path averaged from five stations during the year, and the correlation coefficient between the two daily mean time series is 0.72. The daily mean cloud optical properties derived from CRM-produced liquid and ice water paths have a correlation coefficient of 0.64 with the cloud optical properties retrieved from the ARM measurements at the central facility. This general agreement partially validates the CRM-produced year-long cloud ice water. The comparison with a month-long retrieved cloud ice water path during March 2000 IOP also indicates the CRM did reasonably well in simulating the ice water paths associated with

strong convective events. The CRM-produced cloud ice water path is 50% more than the liquid water path when averaged over the year. It is found that the precipitation and ice clouds have higher correlation with the larger-scale forcing than the surface heat fluxes during spring and summer, while liquid clouds have similar correlations with both the forcing and surface fluxes. During winter, the effects of surface heat fluxes may play a more important role in the simulation of winter clouds, especially near-surface clouds because of the weak large-scale forcing.

The simulated cloud properties exhibit a seasonal variation in response to the varied large-scale forcing and conditions during the year. The peak of the cloud ice water profile reaches the highest level (7 km) associated with the deep convection during summer, and the ice water has a second peak near the surface during winter. The seasonal averaged ice water mixing ratio is twice as large as the liquid water mixing ratio during spring and summer. The cloud liquid water has a single peak around 2 and 4 km during summer and spring, respectively. During late fall and winter, liquid clouds are present near the surface as indicated by the near surface peak in both seasons. Corresponding to the change of ice and liquid clouds, the cloud radiative forcing and the vertical structure of cloud radiative heating rate also indicate a profound seasonal variation. For the shortwave flux at both TOA and the surface, winter has the weakest cloud radiative forcing (cooling effects) over spring, summer, and fall. For the longwave flux, however, different seasonal variations are found at TOA and the surface. The strongest TOA cloud radiative forcing is in spring and summer because of the presence of deeper ice clouds. But the existence of liquid clouds near the surface during winter and late fall leads to the strongest surface longwave cloud radiative forcing. Finally, the effects of clouds on the total radiative heating rate show a dipole pattern with the cooling above 8 km and the heating below during spring and summer. But during fall and winter, the cloud radiative cooling rates appear in two layers with one above 6 km and the other below 2 km, and the heating rate is in between.

While the comparison of a year-long simulation with the observations demonstrates that the cloud systems over the ARM SGP are reasonably generated by the CRM combined with the large-scale forcing and surface heat fluxes, it also reveals the problem that may affect the quality of simulated cloud properties. The use of constant surface albedo is found to be possibly responsible for the difference of surface net shortwave flux between the CRM and observations, although the uncertainties are likely present in obtaining the area mean flux from few stations because of the inhomogeneity of surface conditions. The effects of more realistic surface albedo on the year-long CRM simulation of cloud systems are under investigation. While the overall feature of simulated cloud systems is reproduced by the CRM, the finer structure such as shallow, middle, and high clouds, and their radiative effects, will be evaluated with the improved CRM simulations. Observational studies (Lazarus et al. 2000; Yang et al. 2006) showed that shallow cumulus clouds prominently presented during summer at the ARM SGP may require the CRM with finer grids.

REFERENCES

Cahalan, R. F., W. Ridgway, W. J. Wiscombe, T. L. Bell, and J. B. Snider, 1994: The albedo of fractal stratocumulus clouds. *J. Atmos. Sci.,* **51,** 2434–2455.

Clark, T. L., W. D. Hall, and J. L. Coen, 1996: Source code documentation for the Clark–Hall cloud-scale model: Code version G3CH01. NCAR Tech. Note NCAR/TN-426+STR, 137 pp.

Clothiaux, E. E., T. P. Ackerman, G. G. Mace, K. P. Moran, R. T. Marchand, M. Miller, and B. E. Martner, 2000: Objective determination of cloud heights and radar reflectivities using a combination of active remote sensors at the ARM CART sites. *J. Appl. Meteor.,* **39,** 645–665.

Geleyn, J. F., and A. Hollingsworth, 1979: An economical analytical method for the computation of the interaction between scattering and line absorption of radiation. *Contrib. Atmos. Phys.,* **52,** 1–16.

Ghan, S. J., and Coauthors, 2000: A comparison of single column model simulations of summertime midlatitude continental convection. *J. Geophys. Res.,* **105,** 2091–2124.

Grabowski, W. W., 2001: Coupling cloud processes with the large-scale dynamics using the cloud-resolving convection parameterization (CRCP). *J. Atmos. Sci.,* **58,** 978–997.

——, X. Wu, and M. W. Moncrieff, 1996: Cloud-resolving modeling of tropical cloud systems during Phase III of GATE. Part I: Two-dimensional experiments. *J. Atmos. Sci.,* **53,** 3684–3709.

Heymsfield, A. J., S. Matrosov, and B. Baum, 2003: Ice water

path–optical depth relationships for cirrus and deep strati-form ice cloud layers. *J. Appl. Meteor.,* **42,** 1369–1390.

Holtslag, A. A. M., and C.-H. Moeng, 1991: Eddy diffusivity and countergradient transport in the convective atmospheric boundary layer. *J. Atmos. Sci.,* **48,** 1690–1698.

Hong, S.-Y., and H.-L. Pan, 1996: Nonlocal boundary layer vertical diffusion in a medium-range forecast model. *Mon. Wea. Rev.,* **124,** 2322–2339.

Kessler, E., 1969: *On the Distribution and Continuity of Water Substance in Atmospheric Circulations. Meteor. Monogr.,* No. 32, Amer. Meteor. Soc., 84 pp.

Kiehl, J. T., J. J. Hack, G. B. Bonan, B. A. Boville, B. P. Briegleb, D. L. Williamson, and P. J. Rasch, 1996: Description of the NCAR Community Climate Model (CCM3). NCAR Tech. Note NCAR/TN420+STR, 152 pp. [Available from NCAR, Boulder, CO 80307.]

Koenig, L. R., and F. W. Murray, 1976: Ice-bearing cumulus cloud evolution: Numerical simulation and general comparison against observations. *J. Appl. Meteor.,* **15,** 747–762.

Lau, W. K.-M., and D. E. Waliser, 2005: *Intraseasonal Variability in the Atmosphere–Ocean Climate System.* Springer-Verlag, 436 pp.

Lazarus, S. M., S. K. Krueger, and G. G. Mace, 2000: A cloud climatology of the southern Great Plains ARM CART. *J. Climate,* **13,** 1762–1775.

Li, J., S. Dobbie, P. Räisänen, and Q. Min, 2005: Accounting for unresolved clouds in a 1-D solar radiative-transfer model. *Quart. J. Roy. Meteor. Soc.,* **131,** 1607–1629.

Li, Z., M. C. Cribb, and A. P. Trischenko, 2002: Impact of surface inhomogeneity on solar radiative transfer under overcast conditions. *J. Geophys. Res.,* **107,** 4294, doi:10.1029/2001JD000976.

Liang, X.-Z., and W.-C. Wang, 1997: Cloud overlap effect on general circulation model climate simulations. *J. Geophys. Res.,* **102,** 11 039–11 047.

——, and X. Wu, 2005: Evaluation of a GCM subgrid cloud-radiation interaction parameterization using cloud-resolving model simulations. *Geophys. Res. Lett.,* **32,** L06801, doi:10.1029/2004GL022301.

Mace, G. G., and Coauthors, 2006: Cloud radiative forcing at the Atmospheric Radiation Measurement Program Climate Research Facility: 1. Technique, validation, and comparison to satellite-derived diagnostic quantities. *J. Geophys. Res.,* **111,** D11S90, doi:10.1029/2005JD005921.

Maloney, E. D., and D. L. Hartmann, 2001: The sensitivity of intraseasonal variability in the NCAR CCM3 to changes in convective parameterization. *J. Climate,* **14,** 2015–2034.

Manabe, S., and R. Strickler, 1964: Thermal equilibrium of the atmosphere with a convective adjustment. *J. Atmos. Sci.,* **21,** 361–385.

Miller, M. J., A. C. M. Beljaars, and T. N. Palmer, 1992: The sensitivity of the ECMWF model to the parameterization of evaporation from tropical oceans. *J. Climate,* **5,** 418–434.

Min, Q., and L. Harrison, 1996: Cloud properties derived from surface MFRSR measurements and comparison with GOES results at the ARM SGP site. *Geophys. Res. Lett.,* **23,** 1641–1644.

——, M. Duan, and R. Marchand, 2003: Validation of surface retrieved cloud optical properties with in situ measurements at the Atmospheric Radiation Measurement Program (ARM) South Great Plains site. *J. Geophys. Res.,* **108,** 4547, doi:10.1029/2003JD003385.

——, E. Joseph, and M. Duan, 2004a: Retrievals of thin cloud optical depth from a multifilter rotating shadowband radiometer. *J. Geophys. Res.,* **109,** D02201, doi:10.1029/2003JD003964.

——, P. Minnis, and M. M. Khaiyer, 2004b: Comparison of cirrus optical depths derived from GOES 8 and surface measurements. *J. Geophys. Res.,* **109,** D15207, doi:10.1029/2003JD004390.

Minnis, P., W. L. Smith Jr., D. P. Garber, J. K. Ayers, and D. R. Doelling, 1995: Cloud properties derived from GOES-7 for spring 1994 ARM intensive observing period using version 1.0.0 of ARM satellite data analysis program. NASA Tech. Rep. 1366, 62 pp.

——, ——, D. F. Young, L. Nguyen, A. D. Rapp, P. W. Heck, and M. M. Khaiyer, 2002: Near-real-time retrieval of cloud properties over the ARM CART area from GOES data. *Proc. 12th Atmospheric Radiation Measurement (ARM) Science Team Meeting,* St. Petersburg, FL. [Available online at http://www.arm.gov/publications/proceedings/conf12/extended_abs/minnis-p.pdf.]

Randall, D. A., M. F. Khairoutdinov, A. Arakawa, and W. W. Grabowski, 2003: Breaking the cloud parameterization deadlock. *Bull. Amer. Meteor. Soc.,* **84,** 1547–1564.

Seo, E.-K., and G. Liu, 2005: Retrievals of cloud ice water path by combining ground cloud radar and satellite high-frequency microwave measurements near the ARM SGP site. *J. Geophys. Res.,* **110,** D14203, doi:10.1029/2004JD005727.

Slingo, J. M., and Coauthors, 1994: Mean climate and transience in the tropics of the UGAMP GCM: Sensitivity to convective parameterization. *Quart. J. Roy. Meteor. Soc.,* **120,** 881–922.

——, and Coauthors, 1996: Intraseasonal oscillations in 15 atmospheric general circulation models: Results from an AMIP diagnostic subproject. *Climate Dyn.,* **12,** 325–357.

Smagorinsky, J., 1963: General circulation experiments with the primitive equations. I. The basic experiment. *Mon. Wea. Rev.,* **91,** 99–164.

Stephens, G. L., 1978: Radiation profiles in extended water clouds. II: Parameterization schemes. *J. Atmos. Sci.,* **35,** 2123–2132.

——, 1984: The parameterization of radiation for numerical weather prediction and climate models. *Mon. Wea. Rev.,* **112,** 826–867.

Troen, I., and L. Mahrt, 1986: A simple model of the atmospheric boundary layer: Sensitivity to surface evaporation. *Bound.-Layer Meteor.,* **37,** 129–148.

Wu, X., and M. W. Moncrieff, 2001: Long-term behavior of cloud systems in TOGA COARE and their interactions with radiative and surface processes. Part III: Effects on the energy budget and SST. *J. Atmos. Sci.,* **58,** 1155–1168.

——, and X.-Z. Liang, 2005: Effect of subgrid cloud-radiation interaction on climate simulations. *Geophys. Res. Lett.,* **32,** L24806, doi:10.1029/2005GL024432.

——, W. W. Grabowski, and M. W. Moncrieff, 1998: Long-term behavior of cloud systems in TOGA COARE and their interactions with radiative and surface processes. Part I: Two-dimensional modeling study. *J. Atmos. Sci.,* **55,** 2693–2714.

——, W. D. Hall, W. W. Grabowski, M. W. Moncrieff, W. D. Collins, and J. T. Kiehl, 1999: Long-term behavior of cloud systems in TOGA COARE and their interactions with radiative and surface processes. Part II: Effects of ice microphysics on cloud–radiation interaction. *J. Atmos. Sci.,* **56,** 3177–3195.

——, M. W. Moncrieff, and K. A. Emanuel, 2000: Evaluation of large-scale forcing during TOGA COARE for cloud-

resolving models and single-column models. *J. Atmos. Sci.,* **57,** 2977–2985.

——, X.-Z. Liang, and G. J. Zhang, 2003: Seasonal migration of ITCZ precipitation across the equator: Why can't GCMs simulate it? *Geophys. Res. Lett.,* **30,** 1824, doi:10.1029/2003GL017198.

——, L. Deng, X. Song, G. Vettoretti, W. R. Peltier, and G. J. Zhang, 2007a: Impact of a modified convective scheme on the Madden-Julian Oscillation and El Niño–Southern Oscillation in a coupled climate model. *Geophys. Res. Lett.,* **34,** L16823, doi:10.1029/2007GL030637.

——, ——, ——, and G. J. Zhang, 2007b: Coupling of convective momentum transport with convective heating in global climate simulations. *J. Atmos. Sci.,* **64,** 1334–1349.

——, X.-Z. Liang, and S. Park, 2007c: Cloud-resolving model simulations over the ARM SGP. *Mon. Wea. Rev.,* **135,** 2841–2853.

Xie, S., R. T. Cederwall, and M. Zhang, 2004: Developing long-term single-column model/cloud system–resolving model forcing data using numerical weather prediction products constrained by surface and top of the atmo-

sphere observations. *J. Geophys. Res.,* **109,** D01104, doi:10.1029/2003JD004045.

Yang, F., H.-L. Pan, S. K. Krueger, S. Moorthi, and S. J. Lord, 2006: Evaluation of the NCEP Global Forecast System at the ARM SGP site. *Mon. Wea. Rev.,* **134,** 3668–3690.

Zhang, C., 2005: Madden-Julian Oscillation. *Rev. Geophys.,* **43,** RG2003, doi:10.1029/2004RG000158.

Zhang, G. J., and X. Wu, 2003: Convective momentum transport and perturbation pressure field from a cloud-resolving model simulation. *J. Atmos. Sci.,* **60,** 1120–1139.

——, J. T. Kiehl, and P. J. Rasch, 1998: Response of climate simulation to a new convective parameterization in the National Center for Atmospheric Research Community Climate Model (CCM3). *J. Climate,* **11,** 2097–2115.

Zhang, Y., W. B. Rossow, A. A. Lacis, V. Oinas, and M. I. Mishchenko, 2004: Calculation of radiative fluxes from the surface to top of atmosphere based on ISCCP and other global data sets: Refinements of the radiative transfer model and the input data. *J. Geophys. Res.,* **109,** D19105, doi:10.1029/2003JD004457.